Predictive Position Synchronization Control of Dual Permanent Magnet Synchronous Motor System Based on Geometric Constraints

Xiuyun Zhang, Zhiwei Sun, Jianyu Chen, Zhibiao Zhao, Tao Liu, and Weijie Hou

***Abstract*—Model predictive control (MPC) mitigates synchronous error accumulation, dynamic response mismatch, and precision-complexity tradeoff in traditional multimotor system. However, constrained numerical solutions in MPC present significant computational challenges. To address this, this article proposes a predictive position synchronization control strategy based on geometric constraints for dual permanent magnet synchronous motor (PMSM) system. First, an incremental MPC framework is constructed, whose embedded integral action not only effectively compensates for short control horizons but also enables high-precision multistep prediction. Second, a cost function incorporating tracking error, synchronous error and control increment is established to derive the current control increment. To reduce computational complexity, a constrained geometric mapping method is proposed: with control horizon $N_c = 1$, current and voltage constraints are mapped to a 2D plane to form a feasible region, converting the optimal control increment solution into determining the tangent point between the cost function's elliptic surface family and this feasible region. Rapidly localizing the tangent via real-time query and calculation of analytical solutions significantly reduces online computational load. Experimental results show the proposed strategy can improve computational efficiency by approximately 47% and dynamic response speed by approximately 57% versus traditional quadratic programming (QP) strategy, resolving the precision-complexity tradeoff in multimotor synchronization while ensuring accuracy.**

***Index Terms*—Continuous control set model predictive control (MPC), geometric constraints, multimotor control, permanent magnet synchronous motor (PMSM).**

Received 15 May 2025; revised 2 August 2025; accepted 26 August 2025. Date of publication 2 September 2025; date of current version 23 December 2025. This work was supported in part by Tianjin Nature Science Foundation under Grant 22JCQNJC01100, in part by Tianjin Applied Basic Research Diversified Investment Project under Grant 22JCZDJC00930, and in part by Tianjin Education Commission Scientific Research Project 2024KJ074. Recommended for publication by Associate Editor R. Kennel. *(Corresponding author: Xiuyun Zhang.)*

Xiuyun Zhang, Zhiwei Sun, Jianyu Chen, and Zhibiao Zhao are with the School of Automation and Electrical Engineering, and Tianjin Key Laboratory of Information Sensing and Intelligent Control, Tianjin University of Technology and Education, Tianjin 300222, China (e-mail: xiuyunz@tju.edu.cn; 0522231033@tute.edu.cn; 0522231067@tute.edu.cn; zhaozhibiao@tute.edu.cn).

Tao Liu is with the School of Electrical Engineering, Tiangong University, Tianjin 300387, China (e-mail: liutao@tiangong.edu.cn).

Weijie Hou is with the Tianjin Key Laboratory of Microgravity and Hypogravity Environment Simulation Technology, Tianjin Institute of Aerospace Mechanical and Electrical Equipment, Tianjin 300301, China (e-mail: 016059@nankai.edu.cn).

Color versions of one or more figures in this article are available at https://doi.org/10.1109/TPEL.2025.3605365.

Digital Object Identifier 10.1109/TPEL.2025.3605365

I. Introduction

HIGH-PRECISION equipment manufacturing imposes stringent requirements on the position synchronization control of dual permanent magnet synchronous motor (PMSM) system [1]. However, the inherent high-order, multivariable, and strong coupling characteristics cause synchronous error accumulation and dynamic response mismatch–bottlenecks in high-precision fields like robotics, etc. Moreover, the traditional methods face a precision-complexity tradeoff [2]. Therefore, how to break through the bottleneck, coordinately optimize dynamic performance and synchronization accuracy, while reducing algorithm complexity and computational load, has become a core issue in this field.

A. State of the Art

Multimotor synchronization control method mainly focuses on two aspects: synchronous error compensation control and synchronous error direct control, as shown in Fig. 1.

Synchronous error compensation control refers to the multimotor synchronization structure incorporating single-motor control algorithms. Uncoupled structures (such as master-slave control (MSC) [3], parallel control (PC) [4]) exhibit weak fault tolerance, limited synchronization accuracy, and inability to balance "high precision" and "low complexity." Coupled structures (such as cross-coupled control (CCC) [5], deviation-coupled control (DCC) [6], virtual main axis control (VMAC) [7], adjacent-coupled control (ACC) [8]) enhance synchronization accuracy and dynamic error sup-pression through bidirectional interaction between motors. However, their accuracy improvement is limited by relying solely on structural enhancements. Therefore, researchers combine advanced algorithms, such as fuzzy control (FC) [9], neural network control (NNC) [10], and sliding mode control (SMC) [11] with the synchronization structure to optimize dual-motor performance, such as the combination of second-order active disturbance rejection control (ADRC) and CCC [12], and adaptive control (AC) and CCC [13]. However, the existing schemes have key limitations: First, they insufficiently account for the details of multimotor strong coupling models, resulting in strong coupling in control loops and a sharp rise in parameter tuning dimensions, making the algorithm difficult to simplify. Second, the separate "single-motor optimization + synchronization structure compensation"

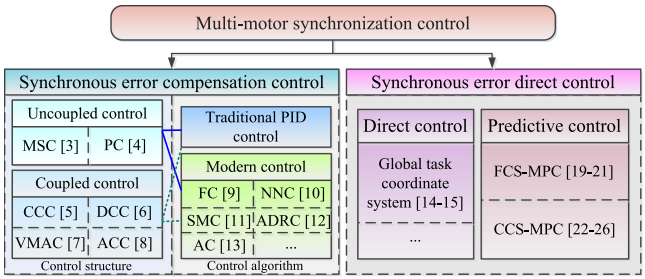

Fig. 1. Research focus of multimotor synchronization control.

design is a post-compensation mechanism. It has inherent lag, restricts performance improvement, and cannot balance the core requirement of "high precision" and "low complexity".

Therefore, researchers propose an integrated position synchronization control algorithm, the core of which is to abandon the separate mode and directly incorporate synchronous error into the multimotor control objectives (synchronous error direct control). This method overcomes traditional limitations, for example, the methods in [14] and [15] achieved integrated synchronous contour control via a global task coordinate system and adaptive robust control, integrating inter-axis coordination and redundant actuator synchronization to overcome inherent lag. Yet, such integrated methods still have drawbacks: First, they lack dynamic prediction capability and fail to pre-suppress disturbances' impact on synchronization accuracy. Second, their computational amount increases exponentially with motor number, complicating engineering implementation and hindering real-time control requirements.

MPC, with its ability to predict synchronous error in advance, multivariable synchronization optimization characteristics, and advantages of rolling horizon dynamic adjustment, shows significant potential beyond traditional methods in multimotor synchronization control: Its predictive mechanism avoids the inherent lag of post-compensation; its multivariable coordination naturally suits multimotor systems' strong coupling characteristics; its rolling optimization dynamically handles requirements in complex conditions. Related explorations have preliminarily verified their effectiveness. For example, Zhang et al. [16] modeled multiple motors based on a multi-input multioutput structure, obtaining the optimal output by solving the cost function or selecting the optimal voltage vector to accelerate error convergence. Building on this, Niu et al. [17] proposed a collaborative predictive position control method, achieving multivariable optimization covering acceleration, constant speed, deceleration, and position approach stages. To address coupling characteristics of nonlinear systems, Zhou et al.[18] constructed a dual-axis nonlinear MPC framework that dynamically tracks and compensates for contour error via an axial coordination mechanism, while introducing a cost function to balance high tracking accuracy and the need to meet control quantity constraints. These methods not only realize predictive control of synchronous error, but also achieve optimal control through unified modeling.

However, MPC algorithms still have certain technical limitations, mainly reflected in the following aspects: For constrained optimal control problems, online solving faces significant computational challenges. In multimotor scenarios, as the number of motors increases, the number of constraints also grows, making this problem more prominent. How to construct an engineering-friendly constraint handling strategy while ensuring real-time performance remains a technical bottleneck to be broken through. In finite control set MPC (FCS-MPC) [19], input constraints mainly come from two aspects. First, the fixed amplitude and direction of optional voltage vectors can directly limit the optional input voltage range in the optimization process [20]. Second, input voltage constraints can be designed as objective function terms (e.g., current limiting [21]) and integrated into the cost function to achieve direct constraints on state variables. Although such constraint integration is relatively simple in solution, FCS-MPC's inadequate steady-state performance hinders its wide application in position synchronization control.

In contrast, continuous control set MPC (CCS-MPC) is more suitable for high-precision synchronization control due to its continuous voltage output characteristics [22]. Its core advantage lies in multivariable rolling horizon prediction capability–it constructs a high-precision dynamic model to predict the future state of the system and dynamically optimizes the control sequence to achieve global optimization of trajectory tracking and resource allocation [23]. From the perspective of the mathematical characteristics of algorithm design, unconstrained optimization problems are usually easy to obtain explicit optimal solutions. However, for constrained CCS-MPC, its cost function generally adopts a quadratic programming (QP) framework. It constructs strictly convex optimization problems by introducing linear or quadratic constraints. This method's evolution follows a clear iterative optimization trajectory: The active set method first enabled engineering solutions to QP problems. By iteratively identifying 'active constraints' to simplify problem dimensions, it is extremely sensitive to constraint count: more system constraints cause frequent active set updates, sharply reducing iteration efficiency–a notable drawback in complex dynamic scenarios [24]. To address its limitations in handling large-scale constraints, the interior point method was proposed. Its innovation is introducing a logarithmic barrier function to shift optimization from constraint boundaries to the feasible region's interior, significantly improving numerical stability and adapting better to large-scale constraints than the active set method, thus alleviating the efficiency bottleneck in multiconstraint scenarios [25]. Subsequent Karush–Kuhn–Tucker-based strategies further integrate modern optimization theory, constructing Lagrangian functions to convert inequality constraints into complementary slackness conditions and theoretically simplifying complex constraint processing logic [26]. Although QP problems under linear constraints have theoretically efficient solution paths, they still essentially rely on the scale of constraints. When motor number increases, the number of constraints rises accordingly, the aforementioned iterative numerical methods still cannot avoid the dilemma of exponentially increasing computational complexity. The resulting massive computational burden not only imposes strict requirements on the hardware computing power

of real-time control systems, but also poses severe challenges to the robustness of algorithms in high-dynamic scenarios.

B. Contribution of This Article

Based on the above analysis, the research focus of this article is primarily on providing a lightweight solution method for real-time dual-motor control scenarios. This article proposes a geometrically constrained predictive position synchronization control strategy for dual PMSM system. More precisely, the contribution includes these key elements.

1) To address the issues of synchronous error accumulation and dynamic response mismatch caused by strong coupling in multimotor system, an incremental MPC framework is constructed. Leveraging its built-in integral action to compensate for the limitations of short control horizons, this framework enables high-precision multistep prediction of position and velocity. Moreover, current control increment is solved by a cost function incorporating tracking error, synchronous error.
2) To address high computational complexity and slow convergence, an innovative constraint geometric mapping method is proposed: When the control horizon is $N_c = 1$, the x- and y-motor current constraints are represented as rectangular regions in a plane, with $\Delta i_{qx}(k)$, $\Delta i_{qy}(k)$ as horizontal and vertical coordinates, respectively. The cost function is then regarded as a family of equivariant surfaces. At this point, the solution of the optimal control increment is transformed into a problem of determining the tangent point between the family of cost function elliptic surfaces and the feasible region.
3) By calculating the tangency points between the elliptical surface and the constrained feasible region, and summarizing them in tabular form, the optimal output solution is then obtained through real-time query and calculation of analytical solutions. The computation time is reduced by approximately 47% compared with the traditional QP algorithm.

II. Mathematical Modeling of Dual PMSM System

In this article, the surface-mounted PMSM is selected, and the motion equation is

$$\begin{cases} J_i \frac{d\omega_i}{dt} = K_{ti} i_{qi} - T_{Li} - B_i \omega_i \\ \frac{d\theta_i}{dt} = \omega_i \end{cases} \tag{1}$$

where J_i is rotational inertia; K_{ti} is torque coefficient of PMSM, and $K_{ti} = 1.5 p_i \psi_{fi}$; i_{qi} is q-axis current; T_{Li} is load torque; B_i is frictional coefficient; ω_i is mechanical angular speed; and θ_i is rotor angle position; where $i = x, y, x$, and y represent x and y motors, respectively.

Discretizing (1) yields

$$\begin{cases} \omega_i(k+1) = (1 - \frac{T_s B_i}{J_i})\omega_i(k) + \frac{T_s K_{ti} i_{q_i}(k)}{J_i} - \frac{T_s T_{Li}}{J_i} \\ \theta_i(k+1) = T_s \cdot \omega_i(k) + \theta_i(k) \end{cases} \tag{2}$$

where T_s represents the control period.

Let $\boldsymbol{x}_i = \begin{bmatrix} \omega_i \\ \theta_i \end{bmatrix}$, $\boldsymbol{y}_i = \theta_i$, it can be obtained

$$\begin{aligned} \begin{bmatrix} \omega_i(k+1) \\ \theta_i(k+1) \end{bmatrix} &= \begin{bmatrix} 1 - \frac{T_s}{J_i} & 0 \\ T_s & 1 \end{bmatrix} \begin{bmatrix} \omega_i(k) \\ \theta_i(k) \end{bmatrix} \\ &+ \begin{bmatrix} \frac{T_s K_{ti}}{J_i} \\ 0 \end{bmatrix} i_{q_i}(k) + \begin{bmatrix} \frac{-T_s T_{Li}}{J_i} \\ 0 \end{bmatrix}. \end{aligned} \tag{3}$$

Rearrange (3) as

$$\begin{cases} \boldsymbol{x}_i(k+1) = \boldsymbol{a}_i \boldsymbol{x}_i(k) + \boldsymbol{b}_i i_q(k) + \boldsymbol{e}_i \\ \boldsymbol{y}_i(k) = \boldsymbol{c}_i \boldsymbol{x}_i(k) \end{cases} \tag{4}$$

where, $\boldsymbol{a}_i = \begin{bmatrix} \mathbf{1} - \frac{T_s B_i}{J_i} & \mathbf{0} \\ \mathbf{T_s} & \mathbf{1} \end{bmatrix}$ $\boldsymbol{b}_i = \begin{bmatrix} \frac{T_s K_{ti}}{J_i} \\ \mathbf{0} \end{bmatrix}$, $\boldsymbol{e}_i = \begin{bmatrix} -\frac{T_s T_{Li}}{J_i} \\ \mathbf{0} \end{bmatrix}$, $\boldsymbol{c}_i = \begin{bmatrix} 0 & 1 \end{bmatrix}$.

At this point, the influence of parametric uncertainties is not taken into account. To incorporate the effects of parametric uncertainties, the equivalent inertia and friction coefficient are defined as follows: $J_{\mathrm{eq}i} = J_i + \Delta J_i$, $B_{\mathrm{eq}i} = B_i + \Delta B_i$, $\psi_{f\mathrm{eq}i} = \psi_{\mathrm{f}i} + \Delta\psi_{fi}$, where ΔJ_{i}, ΔB_i, and $\Delta\psi_{fi}$ represent the uncertainties in inertia, friction coefficient, and flux linkage, respectively.

Disturbances induced by ΔJ_i, ΔB_i, and $\Delta\psi_{fi}$ are modeled as constant or slowly time-varying disturbances that incorporate parametric variations. Coupled with load disturbance effects, they are denoted as ${\mu_i}^d$. Hence, the state equations can be expressed as

$$\begin{cases} \boldsymbol{x}_i(k+1) = \boldsymbol{a}_i \boldsymbol{x}_i(k) + \boldsymbol{b}_i i_q(k) + \boldsymbol{\mu}_i^d \\ \boldsymbol{y}_i(k) = \boldsymbol{c}_i \boldsymbol{x}_i(k) \end{cases}. \tag{5}$$

Since the system's equivalent inertia $J_{\mathrm{eq}i}$, equivalent friction coefficient $B_{\mathrm{eq}i}$, and flux linkage $\psi_{f\mathrm{eq}i}$ are difficult to measure directly, the constant and slowly time-varying disturbance terms ${\mu_i}^d$ in (5) are usually not directly obtainable. It would lead to an increase in the prediction error of the predictive model when ignoring these disturbance terms during the prediction process. To address the problem, the method is embedding an integral term in the predictive model. Replace k with $k-1$, the following can be obtained as

$$\begin{cases} \boldsymbol{x}_i(k) = \boldsymbol{a}_i \boldsymbol{x}_i(k-1) + \boldsymbol{b}_i i_{q_i}(k-1) + \boldsymbol{\mu}_i^d \\ \boldsymbol{y}_i(k-1) = \boldsymbol{c}_i \boldsymbol{x}_i(k-1) \end{cases}. \tag{6}$$

Subtracting (5) from (6) yields

$$\begin{cases} \boldsymbol{x}_i(k+1) - \boldsymbol{x}_i(k) = \boldsymbol{a}_i(\boldsymbol{x}_i(k) - \boldsymbol{x}_i(k-1)) \\ + \boldsymbol{b}_i(i_{q_i}(k) - i_{q_i}(k-1)) \\ \boldsymbol{y}_i(k) - \boldsymbol{y}_i(k-1) = \boldsymbol{c}_i(\boldsymbol{x}_i(k) - \boldsymbol{x}_i(k-1)) \end{cases}. \tag{7}$$

Rearrange (7) as follows:

$$\begin{cases} \Delta\boldsymbol{x}_i(k+1) = \boldsymbol{a}_i \Delta\boldsymbol{x}_i(k) + \boldsymbol{b}_i \Delta i_{q_i}(k) \\ \Delta\boldsymbol{y}_i(k) = \boldsymbol{c}_i \Delta\boldsymbol{x}_i(k) \end{cases} \tag{8}$$

where $\Delta\boldsymbol{x}_i(k+1) = \boldsymbol{x}_i(k+1) - \boldsymbol{x}_i(k)$, $\Delta\boldsymbol{x}_i(k) = \boldsymbol{x}_i(k) - \boldsymbol{x}_i(k-1)$,
$\Delta\boldsymbol{y}_i(k) = \boldsymbol{y}_i(k) - \boldsymbol{y}_i(k-1)$

By introducing the incremental model, that is, embedding an integral term, the unknown constant and slowly time-varying disturbances can be suppressed. This means that when there are

minor modeling errors, the closed loop system exhibits a certain degree of robustness.

By defining $x_{\mathrm{m}i} = [\Delta x_i{}^T(k)\ y_i{}^T(k)]^T = [\Delta\omega_i\ \Delta\theta_i\ \theta_i]^T$, the mathematical model of the modified motor is

$$\begin{cases} \boldsymbol{x}_{mi}(k+1) = \boldsymbol{A}_i\boldsymbol{x}_{mi}(k) + \boldsymbol{B}_i i_{qi}(k) \\ \boldsymbol{y}_{mi}(k) = \boldsymbol{C}_i\boldsymbol{x}_{mi}(k) \end{cases} \tag{9}$$

where

$$\boldsymbol{A}_i = \begin{bmatrix} \boldsymbol{a}_i & 0 \\ \boldsymbol{c}_i\boldsymbol{a}_i & \boldsymbol{I}_{1\times 1} \end{bmatrix}, \quad \boldsymbol{B}_i = \begin{bmatrix} \boldsymbol{b}_i \\ \boldsymbol{c}_i\boldsymbol{b}_i \end{bmatrix}, \quad \boldsymbol{C}_i = \begin{bmatrix} 0 & 0 & 1 \end{bmatrix},$$

$\boldsymbol{c}_i\boldsymbol{a}_i = [T_{\mathbf{s}} \quad 1]$, $\boldsymbol{c}_i\boldsymbol{b}_i = 0$.

So the model of dual motor system is

$$\begin{cases} \boldsymbol{X}(k+1) = \boldsymbol{A}'\boldsymbol{X}(k) + \boldsymbol{B}'\Delta\boldsymbol{u}(k) \\ \boldsymbol{Y}(k+1) = \boldsymbol{C}'\boldsymbol{X}(k) \end{cases}$$

$$\boldsymbol{X}(\boldsymbol{k}) = [\boldsymbol{x}_{mx}^T(k) \quad \boldsymbol{x}_{my}^T(k)]^T$$

$$\boldsymbol{Y}(\boldsymbol{k}) = [\boldsymbol{y}_{mx}(k) \quad \boldsymbol{y}_{my}(k)]^T \tag{10}$$

where

$$\boldsymbol{A'} = \begin{bmatrix} \boldsymbol{A}_x & \boldsymbol{0} \\ \boldsymbol{0} & \boldsymbol{A}_y \end{bmatrix}, \quad \boldsymbol{B'} = \begin{bmatrix} \boldsymbol{B}_x & \boldsymbol{0} \\ \boldsymbol{0} & \boldsymbol{B}_y \end{bmatrix}, \quad \boldsymbol{C'} = \begin{bmatrix} \boldsymbol{C}_x & \boldsymbol{0} \\ \boldsymbol{0} & \boldsymbol{C}_y \end{bmatrix}.$$

Equation (10) represents the model of the dual-motor system. Moreover, this algorithm can be readily extended to multimotor system by simply expanding the dimensions of the matrices $\boldsymbol{A'}$, $\boldsymbol{B'}$, $\boldsymbol{C'}$ accordingly.

To enhance the system dynamic performance, MPC is adopted to predict the system output over multiple steps. By setting the controlling domain as N_c and the predicting domain as N_p ($N_c \le N_p$), it is possible to obtain

$$\begin{aligned} \boldsymbol{Y'} &= \begin{bmatrix} \boldsymbol{Y}(k+1) & \boldsymbol{Y}(k+2) & \cdots & \boldsymbol{Y}(k+N_p) \end{bmatrix}^T \\ \Delta\boldsymbol{I}_q &= \begin{bmatrix} \Delta\boldsymbol{u}(k) & \Delta\boldsymbol{u}(k+1) & \cdots & \Delta\boldsymbol{u}(k+N_c-1) \end{bmatrix}^T. \end{aligned} \tag{11}$$

Based on (11), it is possible to obtain

$$\boldsymbol{Y'} = \boldsymbol{F}\boldsymbol{X}(k) + \boldsymbol{G}\Delta\boldsymbol{i}_q \tag{12}$$

where

$$\boldsymbol{F} = [\boldsymbol{C'A'} \ \ \boldsymbol{C'A'}^2 \ \ \ldots \ \ \boldsymbol{C'A'}^{N_P}]^T$$

$$\boldsymbol{G} = \begin{bmatrix} \boldsymbol{C'B'} & 0 & \cdots & 0 \\ \boldsymbol{C'A'B'} & \boldsymbol{C'B'} & \cdots & 0 \\ \vdots & \vdots & \ddots & \vdots \\ \boldsymbol{C'A'}^{N_p-1}\boldsymbol{B'} & \boldsymbol{C'A'}^{N_p-2}\boldsymbol{B'} & \cdots & \boldsymbol{C'A'}^{N_p-N_c}\boldsymbol{B'} \end{bmatrix}.$$

III. Proposed Control Structure

A. Cost Function

To improve the system synchronization control accuracy, the position synchronous error is incorporated into the cost function. Tracking error e_i refers to the deviation, at any given instant, between the commanded position $\theta_i{}^*$ and the actual position θ_i of a single motor (where $i = x$ or y), expressed as $e_i = \theta_i{}^* - \theta_i$. This error quantifies the motor's precision in following the commanded trajectory. Synchronous error ε refers to the difference, at the same instant, between the actual positions θ_x and θ_y of the two motors, expressed as $\varepsilon = \theta_x - \theta_y$. This error directly measures the precision of synchronization motion between the two motors. Therefore, the cost function is selected as

$$\begin{aligned} J = &(\boldsymbol{R}-\boldsymbol{Y'})^T\boldsymbol{L}^T\boldsymbol{Q}_c\boldsymbol{L}(\boldsymbol{R}-\boldsymbol{Y'}) + (\boldsymbol{R}-\boldsymbol{Y'})^T\boldsymbol{Q}_a(\boldsymbol{R}-\boldsymbol{Y'}) \\ &+ \Delta\boldsymbol{i}_q{}^T\boldsymbol{Q}_u\Delta\boldsymbol{i}_q \end{aligned} \tag{13}$$

where, $\boldsymbol{L} = \begin{bmatrix} L_1 & L_2 & 0 & \cdots & \cdots & \cdots & \cdots & 0 \\ 0 & 0 & L_1 & L_2 & \cdots & \cdots & \cdots & 0 \\ & & & \vdots & \vdots & & & \\ 0 & 0 & 0 & 0 & \cdots & \cdots & L_1 & L_2 \end{bmatrix}_{N_p\times 2N_p}$.

$\boldsymbol{Q_c}$, $\boldsymbol{Q_a}$ are the coefficient matrixes of synchronous error and tracking error respectively, $\boldsymbol{Q_u}$ is the coefficient matrix of control increment.

$$\boldsymbol{R} = [\theta_x^*(k+1)\ \ \theta_y^*(k+1)\ \ \theta_x^*(k+2)\ \ \theta_y^*(k+2)\cdots]^T$$

$$\boldsymbol{Q}_c = k_c \cdot I_{N_p\times N_p},$$

$$\boldsymbol{Q}_a = \begin{bmatrix} \mathrm{diag}[k_{\theta x}, k_{\theta y}], & \cdots, & \mathrm{diag}[k_{\theta x}, k_{\theta y}] \end{bmatrix}_{2N_p\times 2N_p}$$

$$\boldsymbol{Q}_u = k_u I_{2N_c\times 2N_c}.$$

where k_c, $k_{\theta x}$, $k_{\theta y}$, and k_u represent the weight coefficients for synchronous error, x-motor tracking error, y-motor tracking error, and the control increment, respectively. When k_c increases, the synchronous error term plays a relatively stronger role than the tracking error term. This reduces synchronous error and accelerates dynamic response speed, but an excessively large k_c may lead to degraded tracking performance due to over-emphasis on synchronization performance, along with increased speed oscillation and current ripple. Conversely, the synchronous error term plays a relatively weaker role than the tracking error term. When it is extended to multimotor system, the matrices $\boldsymbol{Q_c}$, $\boldsymbol{Q_a}$, and $\boldsymbol{Q_u}$ also need to be expanded in terms of their dimensions accordingly.

Substituting the prediction equation and solving for the control variables, set $\frac{\partial J}{\partial \Delta \boldsymbol{i}_q} = 0$, it is possible to obtain as

$$\begin{aligned} \Delta\boldsymbol{i}_q{}^* = &[\boldsymbol{G}^T\boldsymbol{L}^T\boldsymbol{Q}_c\boldsymbol{L}\boldsymbol{G} + \boldsymbol{G}^T\boldsymbol{Q}_a\boldsymbol{G} + \boldsymbol{Q}_u]^{-1}\boldsymbol{G}^T[\boldsymbol{L}^T\boldsymbol{Q_c}\boldsymbol{L} \\ &+ \boldsymbol{Q}_a]\cdot[\boldsymbol{R} - \boldsymbol{F}\boldsymbol{X}(k)]. \end{aligned} \tag{14}$$

The control amount predicted by the model at the current time is

$$\boldsymbol{i}_q(k) = \Delta\boldsymbol{i}_q{}^*(k) + \boldsymbol{i}_q(k-1). \tag{15}$$

B. Constraint Condition

In practical PMSM systems, constrained by the rated output current as well as the maximum voltage and current limits of the motor itself, the stator current and voltage of the PMSM must satisfy the following constraints (taking the x-motor as an example)

$$i_{sx}^2(k+1) = i_{dx}^2(k+1) + i_{qx}^2(k+1) \le i_{\max x}^2 \tag{16}$$

$$u_{dx}^2(k+1)+u_{qx}^2(k+1) \le u_{\max x}^2 = \left(\frac{1}{\sqrt{3}}U_{dc}\right)^2 \tag{17}$$

where $i_{dx}(k+1)$, $i_{qx}(k+1)$ is the predicted d and q-axes currents at moment $k+1$, $i_{\max x}$ is the maximum current, $u_{dx}(k+1)$, $u_{qx}(k+1)$ are the d and q-axes voltages at moment $k+1$, $U_{\rm dc}$ is the dc-side voltage.

To determine the current limiting values for PMSM operation at different speeds, the calculations are typically performed separately for speeds both above and below the base speed, according to [16].

1) When the motor speed ω_x is less than the base speed $\omega_{\rm basex}$, the motor operating state is limited only by $i_{\max x}$. At this point, the limit value of i_{qx} is $i_{qx\max 1} = i_{\max x}$.
2) When the motor speed ω_x is greater than the base speed $\omega_{\rm base\,x}$, at this time, the motor operating state is limited by $i_{\rm maxx}$ and $u_{\rm maxx}$ together. For the surface-mounted PMSM, $L_{dx} = L_{qx}$, the corresponding d- and q-axes currents can be determined as

$$\begin{cases} i_{dx\max 2} = \dfrac{\sqrt{(u_{\max x}/\omega_x)^2-(L_{qx}i_{qx})^2}-\psi_{fx}}{L_{dx}} \\ i_{qx\max 2} = \sqrt{i_{\max x}^2 - i_{dx\max 2}^2} \end{cases}. \tag{18}$$

Therefore, the limits of i_{qx} at different speeds of the PMSM, represented by $i_{{\rm con}x}$, are synthesised by combining $i_{qx\max 1}$ and $i_{qx\max 2}$

$$\begin{cases} i_{{\rm con}x} = i_{qx\,\max 1} & \text{when } \omega_x \le \omega_{{\rm base}\,x} \\ i_{conx} = i_{qx\,\max 2} & \text{when } \omega_x > \omega_{{\rm base}\,x} \end{cases}. \tag{19}$$

Therefore, the limiting range of $\Delta i_{qx}(k)$ is determined as

$$\begin{cases} \Delta i'_{\min} \le \Delta i_{qx}(k) \le \Delta i'_{\max} \\ \Delta i'_{\min} = -(i_{{\rm con}x} - i_{qx}(k-1)) \\ \Delta i'_{\max} = i_{{\rm con}x} - i_{qx}(k-1) \end{cases}. \tag{20}$$

Similarly, the limits of i_{qy} at different speeds of the PMSM are represented by $i_{\rm cony}$, and the limiting range of $\Delta i_{qy}(k)$ is

$$\begin{cases} \Delta i_{\min} \le \Delta i_{qy}(k) \le \Delta i_{\max} \\ \Delta i_{\min} = -(i_{\rm cony} - i_{qy}(k-1)) \\ \Delta i_{\max} = i_{\rm cony} - i_{qy}(k-1) \end{cases}. \tag{21}$$

C. Optimization Problem Analysis

By substituting (12) into the expression of the cost function J in (13) and combining the solution of the constrained convex optimization problem, the convex optimization model can be represented as

$$\begin{cases} J = \Delta \boldsymbol{i}_q{}^T(\boldsymbol{G}^T\boldsymbol{L}^T\boldsymbol{Q}_c\boldsymbol{L}\boldsymbol{G} + \boldsymbol{G}^T\boldsymbol{Q}_a\boldsymbol{G} + \boldsymbol{Q}_u)\Delta \boldsymbol{i}_q \\ \quad -2\Delta \boldsymbol{i}_q{}^T\boldsymbol{G}^T(\boldsymbol{L}^T\boldsymbol{Q}_c\boldsymbol{L} + \boldsymbol{Q}_a)(\boldsymbol{R} - \boldsymbol{F}\boldsymbol{X}(k)) + c \\ \text{s.t.} \quad \boldsymbol{M}\Delta \boldsymbol{i}_q \le \boldsymbol{\gamma} \\ c = (\boldsymbol{R} - \boldsymbol{F}\boldsymbol{X}(k))^T(\boldsymbol{L}^T\boldsymbol{Q}_c\boldsymbol{L} + \boldsymbol{Q}_a)(\boldsymbol{R} - \boldsymbol{F}\boldsymbol{X}(k)) \end{cases} \tag{22}$$

where $\boldsymbol{M} = \begin{bmatrix} 1 & 0 \\ -1 & 0 \\ 0 & 1 \\ 0 & -1 \end{bmatrix}, \boldsymbol{\gamma} = \begin{bmatrix} i_{{\rm con}x} - i_{qx}(k-1) \\ -(i_{{\rm con}x} - i_{qx}(k-1)) \\ i_{\rm cony} - i_{qy}(k-1) \\ -(i_{\rm cony} - i_{qy}(k-1)) \end{bmatrix}$.

The aforementioned equation can be regarded as a convex optimization problem with constraints or as a linear quadratic programming problem. Herein, c is a constant whose presence or absence does not affect the computation of the system's optimal solution. For constrained quadratic programming problems, the existing solutions involve high computational effort and code complexity, hindering embedded algorithm implementation. To address optimization and prediction-related computational burdens, this article proposes a rapid convex optimization solution via geometric characteristic analysis. Specifically, it first analyzes the geometric distributions of the cost function, system constraints, and constrained solution characteristics in the problem, then designs a corresponding simplified strategy.

According to [27], (20) can be represented as a family of level surfaces in the optimization space $\Delta \boldsymbol{i}_q \in R^N$. In general, the control law exists and is unique; therefore, the real-time optimization problem of the constrained predictive control system can be expressed in the following form:

$$\begin{cases} \min \Delta \boldsymbol{i}_q{}^T(\boldsymbol{G}^T\boldsymbol{L}^T\boldsymbol{Q}_c\boldsymbol{L}\boldsymbol{G} + \boldsymbol{G}^T\boldsymbol{Q}_a\boldsymbol{G} + \boldsymbol{Q}_u)\Delta \boldsymbol{i}_q \\ -2\Delta \boldsymbol{i}_q{}^T\boldsymbol{G}^T(\boldsymbol{L}^T\boldsymbol{Q}_c\boldsymbol{L} + \boldsymbol{Q}_a)(\boldsymbol{R} - \boldsymbol{F}\boldsymbol{X}(k)) + c \\ \text{s.t.} \quad \Delta i'_{\min} \le \Delta i_{qx}(k) \le \Delta i'_{\max}, \Delta i_{\min} \le \Delta i_{qy}(k) \le \Delta i_{\max} \end{cases}. \tag{23}$$

From the aforementioned equation, it can be observed that the equivalent optimization model remains a convex optimization problem that satisfies linear boundary conditions, or in other words, a quadratic programming problem with constraints. Set

$$\begin{aligned} &\boldsymbol{G}^T\boldsymbol{L}^T\boldsymbol{Q}_c\boldsymbol{L}\boldsymbol{G} + \boldsymbol{G}^T\boldsymbol{Q}_a\boldsymbol{G} + \boldsymbol{Q}_u \triangleq \begin{bmatrix} g_{11}+\lambda_1 & g_{12} \\ g_{21} & g_{22}+\lambda_2 \end{bmatrix} \\ &-2\boldsymbol{G}^T(\boldsymbol{L}^T\boldsymbol{Q}_c\boldsymbol{L} + \boldsymbol{Q}_a)(\boldsymbol{R} - \boldsymbol{F}\boldsymbol{X}(k)) = \begin{bmatrix} b_1 \\ b_2 \end{bmatrix}. \end{aligned} \tag{24}$$

It can be seen that $(\boldsymbol{G}^T\boldsymbol{L}^T\boldsymbol{Q}_c\boldsymbol{L}\boldsymbol{G}+\boldsymbol{G}^T\boldsymbol{Q}_a\boldsymbol{G}+\boldsymbol{Q}_u)$ is always positive definite, so the family of level surfaces is as

$$\begin{cases} \min \begin{bmatrix} \Delta \boldsymbol{i}_{qx} \\ \Delta \boldsymbol{i}_{qy} \end{bmatrix}^T \begin{bmatrix} g_{11}+\lambda_1 & g_{12} \\ g_{21} & g_{22}+\lambda_2 \end{bmatrix} \begin{bmatrix} \Delta \boldsymbol{i}_{qx} \\ \Delta \boldsymbol{i}_{qy} \end{bmatrix} + \begin{bmatrix} \Delta \boldsymbol{i}_{qx} \\ \Delta \boldsymbol{i}_{qy} \end{bmatrix}^T \begin{bmatrix} b_1 \\ b_2 \end{bmatrix} + c \\ = (g_{11}+\lambda_1)\Delta \boldsymbol{i}_{qx}^2 + (g_{22}+\lambda_2)\Delta \boldsymbol{i}_{qy}^2 + (g_{12}+g_{21})\Delta \boldsymbol{i}_{qx}\Delta \boldsymbol{i}_{qy} \\ \quad + b_1\Delta \boldsymbol{i}_{qx} + b_2\Delta \boldsymbol{i}_{qy} + c \\ \text{s.t.} \quad \Delta i'_{\min} \le \Delta i_{qx}(k) \le \Delta i'_{\max}, \Delta i_{\min} \le \Delta i_{qy}(k) \le \Delta i_{\max} \end{cases}. \tag{25}$$

The aforementioned isometric surfaces constitute a family of elliptic curves, which form a cluster of elliptic curves with the same center, eccentricity, and inclination in the Δi_{qx}-Δi_{qy} coordinate plane. The distribution of J with the same cost function value lies on the same ellipse. The center of the ellipse, denoted as o_1 in the Δi_{qx}-Δi_{qy} plane, corresponds to the unconstrained global optimal solution $\Delta \boldsymbol{i}_{\rm q}$.

When $N_{\rm c}$ is greater than 1, the dimension of $\boldsymbol{G}^T\boldsymbol{L}^T\boldsymbol{Q}_c\boldsymbol{L}\boldsymbol{G} + \boldsymbol{G}^T\boldsymbol{Q}_a\boldsymbol{G} + \boldsymbol{Q}_u$ becomes $2N_c \times 2N_c$, and the dimension of $\boldsymbol{G}^T[\boldsymbol{L}^T\boldsymbol{Q}_c\boldsymbol{L} + \boldsymbol{Q}_a] \cdot [\boldsymbol{R} - \boldsymbol{F}\boldsymbol{X}(k)]$ is $2N_c \times 1$. So, the decision space expands to $2N_{\rm c}$ dimensions, and the geometric constraint conditions change from a simple circle to the intersection

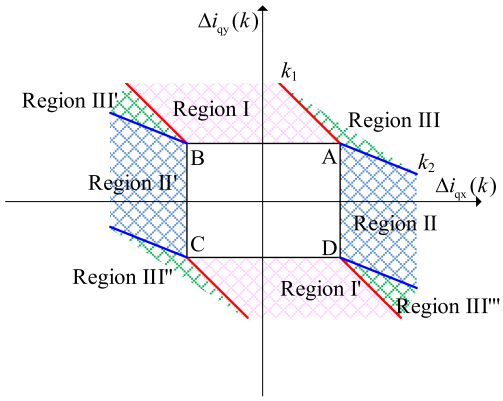

Fig. 2. Constrained feasible domain.

of high-dimensional ellipsoids. At this point, the spatial geometric relationship becomes extremely complex. Theoretically speaking, this requires an expansion of the spatial geometric analysis method.

Moreover, increasing N_c entails scaling up the dimension of the optimization problem by N_c times. This will lead to a substantial rise in computational load, while the marginal gain it offers for performance enhancement is rather limited. In each control cycle, MPC only implements the first control action at the current instant not the entire prediction sequence, which is also validated in the study [28]: "Experiments indicate that the discrepancy in system output is nearly negligible when comparing the consideration of constraints for the discarded portion with the sole consideration of $\Delta \boldsymbol{U}(k)$ constraints." Given these considerations, the control horizon in this article is set to $N_c = 1$. However, the prediction horizon N_p remains larger than 1, which not only retains the predictive ability but also maintains a relatively extended prediction range.

The feasible region is two polygons and their interiors. Fig. 2 illustrates the geometric distribution of the system constraints in (25) within the Δi_{qx}-Δi_{qy} coordinate plane. Therefore, the essence of the optimization problem is to determine when the family of elliptical curves is tangent to the feasible region.

The primary scenarios can be categorized as follows.

Case 1: If $\Delta i_q{}^*$ is located inside the rectangle, it is the optimal solution.

Case 2: If $\Delta i_q{}^*$ falls outside the rectangle, the optimal solution lies on the boundary of the rectangle. The solution is determined based on the specific boundary segment, as shown in Fig. 2, which divides the scenario into three cases.

1) When it is tangent to *AB*, the tangent point is solved as

$$\begin{aligned}\frac{\partial s}{\partial \Delta i_{qx}(k)} &= 2\left(g_{11}+\lambda_1\right)\left(\Delta i_{qx}(k)-\Delta i_{qx}^*(k)\right)\\ &\quad+g_{21}\left(\Delta i_{qy}(k)-\Delta i_{qy}^*(k)\right)\\ &\quad+g_{12}\left(\Delta i_{qy}(k)-\Delta i_{qy}^*(k)\right)=0.\end{aligned}\tag{26}$$

Therefore,

$$\begin{cases}\Delta i_{qx}(k)=\Delta i_{qx}^*(k)+\frac{g_{12}}{g_{11}+\lambda_1}\left(\Delta i_{qy}^*(k)-\Delta i_{\max}\right)\\ \Delta i_{qy}(k)=\Delta i_{\max}\end{cases}.\tag{27}$$

TABLE I
CONSTRAINT VALUES FOR REGION I AND REGION I'

Region	I	I'
Δi_{qx}	(27)	(27)
Δi_{qy}	$\Delta i_{\max}$	$\Delta i_{\min}$

If the tangent point is on AB, just $\Delta i'_{\min} \le \Delta i_{qx}(k) \le \Delta i'_{\max}$ needs to be satisfied, so

$$\begin{aligned}&\Delta i_{qx}^*(k)+\frac{g_{12}}{g_{11}+\lambda_1}\Delta i_{qy}^*(k)\\ &\le \Delta i'_{\max}+\frac{g_{12}}{g_{11}+\lambda_1}\Delta i_{\max}\\ &\Delta i_{qx}^*(k)+\frac{g_{12}}{g_{11}+\lambda_1}\Delta i_{qy}^*(k)\\ &\ge \Delta i'_{\min}+\frac{g_{12}}{g_{11}+\lambda_1}\Delta i_{\max}.\end{aligned}\tag{28}$$

When the equal sign is true, the above equations are straight lines with slope $k_1 = -\frac{g_{11}+\lambda_1}{g_{12}}$ through *AB*.

Therefore, when $\Delta i_q{}^*$ lies in the region I, the optimal solution is the tangent point.

Similarly, the region I' can be solved, and the optimal solution is the tangent point on CD, namely $\Delta i_{qy}(k) = \Delta i_{\min}$ in (27).

Therefore, in the first case, the corresponding constraint values for regions I and I' are given in Table I.

1) When it is tangent to *AD*, the tangent point is solved as

$$\begin{aligned}\frac{\partial s}{\partial \Delta i_{qy}(k)} &= 2(g_{22}+\lambda_2)(\Delta i_{qy}(k)-\Delta i_{qy}^*(k)\\ &\quad+g_{12}(\Delta i_{qx}(k)-\Delta i_{qx}^*(k))\\ &\quad+g_{21}(\Delta i_{qx}(k)-\Delta i_{qx}^*(k))=0.\end{aligned}\tag{29}$$

Therefore,

$$\begin{cases}\Delta i_{qy}(k)=\Delta i_{qy}^*(k)+\frac{g_{21}}{g_{22}+\lambda_2}\left(\Delta i_{qx}^*(k)-\Delta i'_{\max}\right)\\ \Delta i_{qx}(k)=\Delta i'_{\max}\end{cases}.\tag{30}$$

If the tangent point is on *AD*, just $\Delta i_{\min} \le \Delta i_{qy}(k) \le \Delta i_{\max}$ needs to be satisfied, so

$$\begin{aligned}&\Delta i_{qy}^*(k)+\frac{g_{21}}{g_{22}+\lambda_2}\Delta i_{qx}^*(k)\\ &\le \Delta i_{\max}+\frac{g_{21}}{g_{22}+\lambda_2}\Delta i'_{\max}\\ &\Delta i_{qy}^*(k)+\frac{g_{21}}{g_{22}+\lambda_2}\Delta i_{qx}^*(k)\\ &\ge \Delta i_{\min}+\frac{g_{21}}{g_{22}+\lambda_2}\Delta i'_{\max}.\end{aligned}\tag{31}$$

When the equal sign is true, the above equations are straight lines with slope $k_2 = -\frac{g_{22}+\lambda_2}{g_{21}}$ through *AD*.

Therefore, when $\Delta i_q{}^*$ lies in the region II, the optimal solution is the tangent point.

Similarly, the region II' can be solved, and the optimal solution is the tangent point on *BC*, namely $\Delta i_{qx}(k) = \Delta i'_{\min}$ in (30).

Therefore, in the second case, the corresponding constraint values for regions II and II' are given in Table II.

TABLE II
CONSTRAINT VALUES FOR REGION II AND REGION II'

Region	II	II'
Δi_{qx}	$\Delta i'_{\max}$	$\Delta i'_{\min}$
Δi_{qy}	(30)	(30)

TABLE III
CONSTRAINT VALUES FOR THE FOUR ANGULAR REGIONS

Region	III	III'	III''	III'''
Δi_{qx}	$\Delta i'_{\max}$	$\Delta i'_{\min}$	$\Delta i'_{\min}$	$\Delta i'_{\max}$
Δi_{qy}	$\Delta i_{\max}$	$\Delta i_{\max}$	$\Delta i_{\min}$	$\Delta i_{\min}$

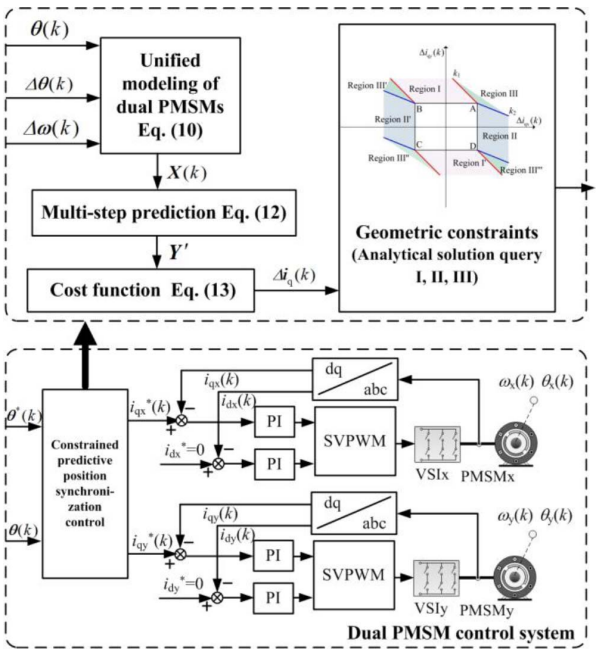

Fig. 3. Block diagram of predictive position synchronization control of dual PMSM system.

Four corner regions: In the plane defined by $\Delta i_{qy}(k)$ and $\Delta i_{qx}(k)$, there are four corner regions. It is evident that when $\Delta i_q{}^*$ is situated within this region, the corner points of the rectangle represent the optimal solutions

$$\begin{cases} \text{Region III} \to A \\ \text{Region III}' \to B \\ \text{Region III}'' \to C \\ \text{Region III}''' \to D \end{cases}. \tag{32}$$

Similarly, the constraint values associated with the four corner regions in the third case are given in Table III.

IV. OVERALL STRUCTURE OF THE CONTROL SYSTEM

The structural diagram depicting the predictive position synchronization control of dual PMSM system based on geometric constraints is illustrated in Fig. 3. Initially, the unconstrained optimal solution for direct predictive position synchronization control is determined via unified modeling of dual motors,

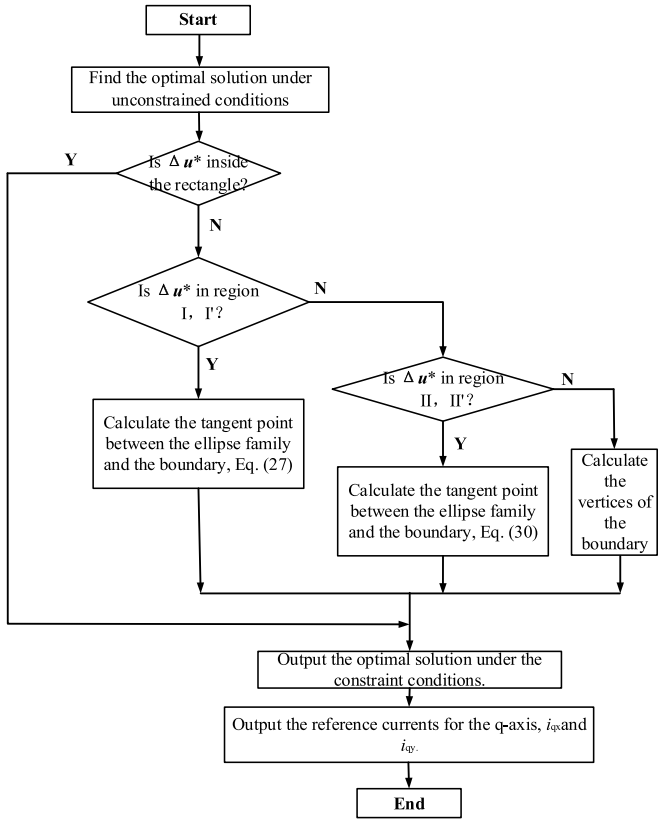

Fig. 4. Algorithm flow chart.

multistep prediction, and resolution of the cost function. Following this, the scenario where $N_c = 1$ is examined, wherein the current constraints for the x-motor and y-motor are represented as rectangular regions in the plane, with $\Delta i_{qx}(k)$, $\Delta i_{qy}(k)$ on horizontal, vertical axis. Within the optimization space, the constrained problem is transformed into a geometric one: identifying tangency points between a family of ellipses and the constraint-defined feasible region. This then requires identifying the position of the control increment within the geometrically constrained region, and the optimal solution under the constraints is obtained by real time query and calculation of analytical solutions. Finally, the control currents necessary for driving the dual PMSMs can be obtained.

The algorithmic implementation flowchart is illustrated in Fig. 4.

Step 1: Formulate the dual PMSM system mathematical model and determine the optimal solution under unconstrained conditions by solving the selected cost function.

Step 2: Based on the current and voltage constraints that the PMSMs must adhere to, calculate the saturation limits of the q-axis currents for both motors. For $N_c = 1$, represent the x-motor and y-motor current constraints as rectangular regions in a plane, with $\Delta i_{qx}(k)$, $\Delta i_{qy}(k)$ on the horizontal and vertical axes, respectively. Then assess whether the center o of the concentric ellipses (representing the unconstrained optimal

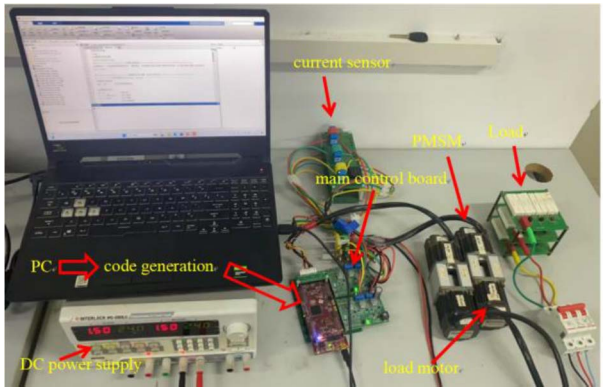

Fig. 5. Experimental platform.

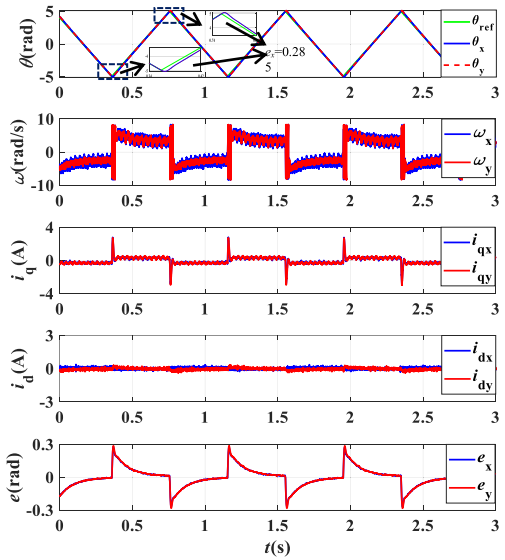

Fig. 6. Result diagram of triangular wave motion trajectory.

solution) lies within the constraint-defined feasible domain. If it does, the solution can be output directly.

Step 3: Determine whether the center o is within regions I and I'. If so, calculate the point of tangency using (27). Otherwise, determine whether the center o is within regions II and II'. If so, calculate the point of tangency using (30). Otherwise, compute the vertices of the boundary.

Step 4: By combining the solved tangency points and vertices, the optimal solution under the constraints is output, and ultimately, the reference currents i_{qx} and i_{qy} of the two motors on the q-axis are obtained.

V. Experimental Studies

A. Experiment System

To validate the control performance of the proposed predictive position synchronization control for the dual PMSM system based on geometric constraints, an experimental platform as depicted in Fig. 5 is constructed. The main control DSP chip adopts the TI floating-point processor TMS320F28379D.

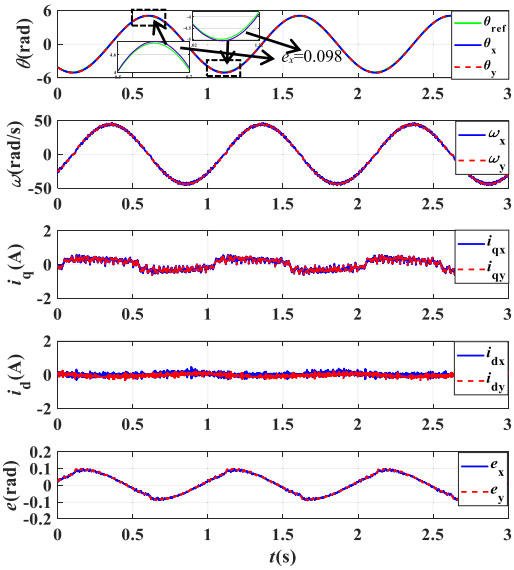

Fig. 7. Result diagram of sine wave trajectory tracking.

TABLE IV
Parameters of Dual PMSMs

MOTOR	PMSM$_x$	PMSM$_y$
U_{dc}/V	24	24
P_N/kW	0.13	0.13
R/Ω	0.345	0.345
L/mH	0.3665	0.3665
p	4	4
n_N/(r/min)	3000	3000
T_N/(N·m)	0.42	0.42
J/(kg·m²)	0.000001	0.000001
B/(N·ms)	0.0001	0.0001
Ψ_f/(Wb)	0.0091521	0.0091521

TMS320F28379D is a highly functional 32-bit floating-point microcontroller unit with an operating main frequency of 200 MHz. It enjoys the merits of high control accuracy and low power consumption, and the control period is 100 μs. The parameters of dual PMSMs are shown in Table IV.

In the verification experiment, the control effect of the proposed method is mainly evaluated by dynamic performance and steady-state performance. Dynamic performance is mainly characterized by maximum tracking error, maximum synchronous error, and dynamic response time. Steady-state performance is mainly characterized by steady-state tracking error and synchronous error.

Among them, the maximum dynamic error is

$$\sigma_{\max} = \max_k(|\sigma(k)|) \tag{33}$$

where $\sigma(k)$ represents $e_x(k)$, $e_y(k)$ and $\epsilon(k)$. $e_x(k)$, $e_y(k)$, and $\epsilon(k)$ are respectively the x-motor tracking error, y-motor tracking error, and synchronous error at time kT_s.

Among them, the average value of the steady-state error is

$$\sigma_{rms} = \sqrt{\frac{\sum_{k=1}^{n_s} \sigma^2(k)}{n_s}} \tag{34}$$

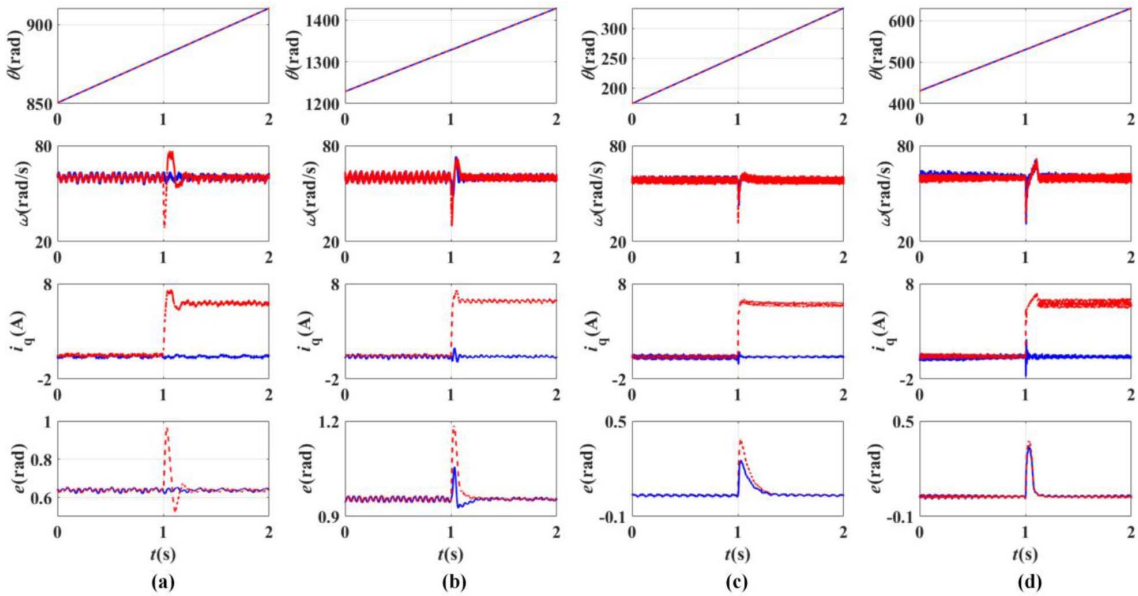

Fig. 8. Control effect diagram when the load changes. (a) Parallel control. (b) Cross-coupled control. (c) QP. (d) Proposed algorithm ($k_c = 500$).

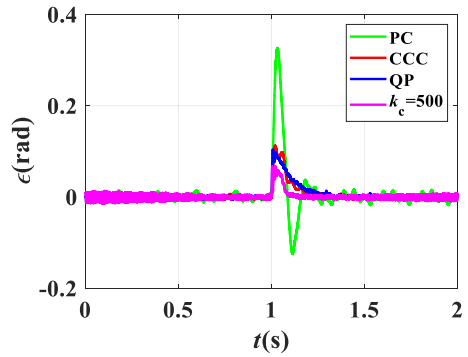

Fig. 9. Synchronous error comparison.

where n_s is the number of steady-state sampling times.

Dynamic response time (t_s) is a key indicator for measuring the dynamic response speed of a system. Its standard definition refers to the minimum time required for the response curve to reach and not exceed the error band of $\pm 5\%$ or $\pm 2\%$ relative to the steady-state line of the response curve.

B. Track the Motion Trajectory of a Triangular Wave

In order to evaluate the control performance of the proposed algorithm in tracking the motion trajectory of a triangular wave, a dual PMSM drive system was configured to follow a piecewise linear trajectory with amplitudes ranging from -5 rad to 5 rad. Fig. 6 illustrates the tracking results obtained from the proposed algorithm, encompassing position, velocity, *d*–*q* axes currents, and tracking errors.

As shown in Fig. 6, the predictive position synchronization control strategy for the dual PMSM system based on geometric constraints demonstrates good performance in tracking the motion trajectory of a triangular wave. Taking the *x*-motor as an example, when the *x*-motor switches between forward and reverse rotation, the maximum tracking error of the *x*-motor is 0.285 rad, indicating a relatively small tracking error. Additionally, the speed and current of the dual-motor system remain relatively stable.

C. Track the Motion Trajectory of a Sine Function Curve

In order to validate the control efficacy of the proposed algorithm in tracking sinusoidal motion trajectories, the dual PMSM drive system was commanded to follow a sinusoidal motion trajectory. Fig. 7 illustrates the tracking results obtained from the proposed algorithm, encompassing position, velocity, *d*–*q* axes currents, and tracking errors.

As illustrated in Fig. 7, the predictive position synchronization control strategy for the dual PMSM system based on geometric constraints exhibits good performance in tracking curved trajectories. Using the *x*-motor as an example, when the *x*-motor switches between forward and reverse rotation, the maximum tracking error of the *x*-motor is 0.098 rad, which indicates a relatively low tracking error. Furthermore, the speed and current of the dual-motor system also remain relatively stable.

D. Validation Through Loading Tests

In order to validate the control effect of the proposed algorithm when it is loaded, the dual PMSM is commanded to track a slanted motion trajectory. This is determined to ascertain whether the control algorithm is capable of maintaining control under load. At 1s, a sudden load is applied to the *x*-motor, while the *y*-motor remains unloaded. The comparative experiments under sudden load are conducted using PC, CCC, QP algorithm, and the proposed control algorithm with synchronous error coefficients of 500, respectively. The control experiment

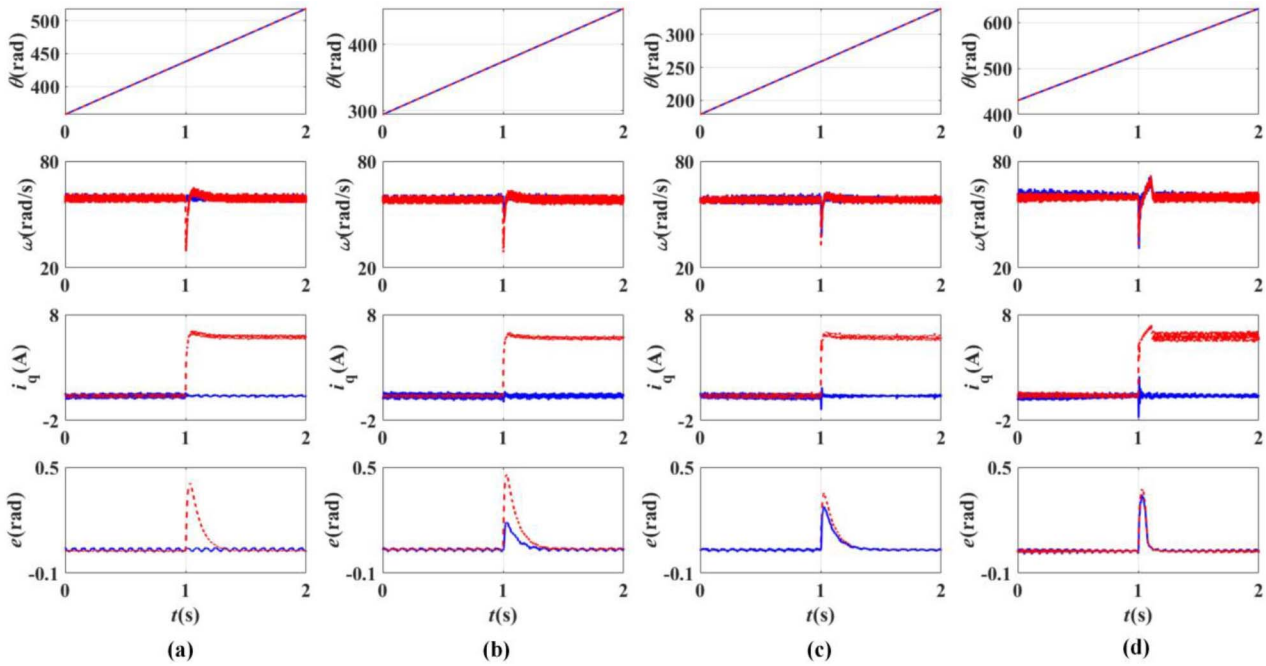

Fig. 10. Control effect diagrams with different synchronous error coefficients. (a) $k_c = 0$. (b) $k_c = 50$. (c) $k_c = 200$. (d) $k_c = 500$.

TABLE V
COMPARISON OF TRACKING ERROR AND SYNCHRONOUS ERROR UNDER THREE STRATEGIES

Comparison items	PC	CCC	QP	Proposed algorithm
$e_{x\max}$	0.961	1.182	0.382	0.371
$e_{y\max}$	0.651	1.052	0.251	0.346
$\epsilon_{\max}$	0.327	0.112	0.131	0.058
t_s of ϵ	0.403	0.303	0.34	0.145
$\epsilon_{\rm rms}$	0.047	0.018	0.026	0.01

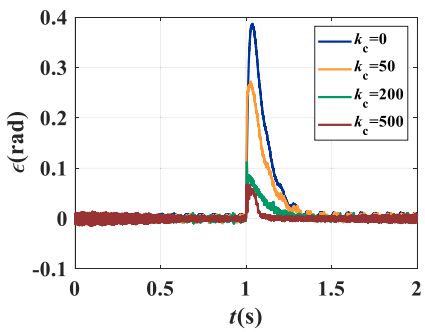

Fig. 11. Synchronous error comparison.

waveforms during load variation are shown in Fig. 8. The blue solid line represents the response curve of the y-motor, and the red dashed line represents the response curve of the x-motor. Fig. 9 shows the comparison of synchronous errors for the four different algorithms. Table V gives the maximum tracking error on x-motor ($e_{x\max}$), the maximum tracking error on y-motor ($e_{y\max}$), the maximum synchronous error ($\epsilon_{\max}$), the average steady-state value of synchronous error($\epsilon_{\rm rms}$), and the dynamic response time (t_s) for the four different algorithms.

Based on the quantitative analysis results given in Table V, the CCC algorithm achieves significant performance improvements in synchronization accuracy and response speed compared to the PC algorithm, with the synchronous error and dynamic response time optimized to 0.112 rad and 0.303 s, respectively. The significant improvement in performance is mainly due to the addition of coupled control structure. Specifically, by introducing a coupling-based collaborative control mechanism into the system, the dual motors achieve real-time interactive compensation of state information. This not only effectively suppresses the cumulative effect of inter-axis motion deviations but also synchronously enhances dynamic tracking accuracy and system response efficiency. When QP algorithm is used, the maximum tracking errors of the x-motor and y-motor using MPC reach 0.382 and 0.251 rad, respectively, which are significantly lower than those of PC and CCC. When the proposed algorithm $k_c = 500$ is used, the maximum synchronous error of MPC is 0.058 rad, and the dynamic response time is 0.145 s, both of which are superior to other methods. It can be seen from the above that after the synchronous error coefficient is introduced, the y-motor will be affected by the loading of the x-motor and change accordingly, that is, the coupling effect of the two motors is introduced. Meanwhile, the execution times of the QP algorithm and the proposed algorithm were measured: the QP algorithm takes 81.35 μs, and the proposed algorithm takes 43.43 μs. In comparison, the proposed algorithm reduces the time by approximately 47% compared with the QP algorithm, with a significant reduction in computational load. Therefore, this proposed control algorithm can reduce the computational burden.

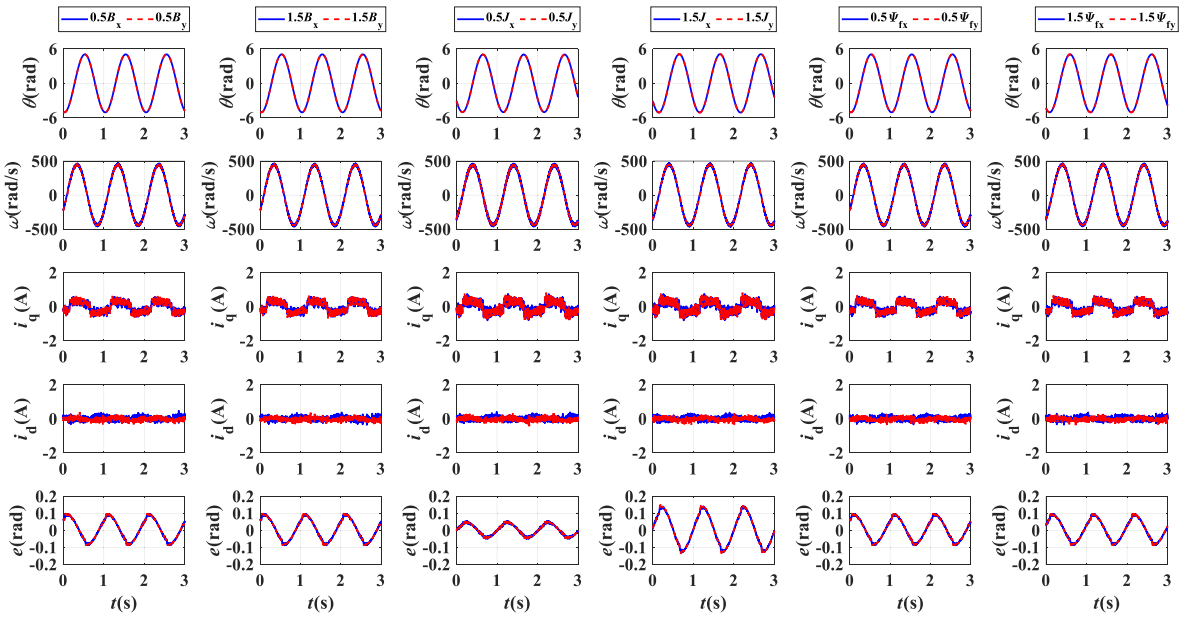

Fig. 12. Control effect chart when parameters change.

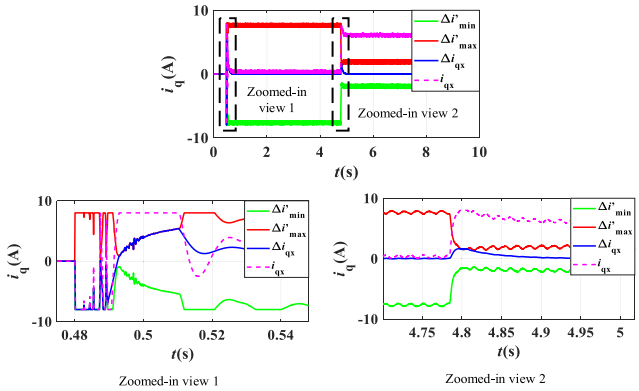

Fig. 13. Constraint on q-axis current increment and q-axis current during startup and loading.

TABLE VI
COMPARISON OF TRACKING ERROR AND SYNCHRONOUS ERROR UNDER DIFFERENT SYNCHRONOUS ERROR COEFFICIENTS

Comparison items	k_c=0	k_c=50	k_c=200	k_c=500
$e_{x\max}$	0.409	0.457	0.354	0.371
$e_{y\max}$	0.041	0.188	0.274	0.346
$\epsilon_{\max}$	0.367	0.269	0.080	0.058
t_s of ϵ	0.339	0.329	0.281	0.145
$\epsilon_{\rm rms}$	0.107	0.053	0.016	0.01

E. Experimental Comparison Under Varying Weight Coefficient Tuning

To validate the control efficacy of the proposed control algorithm under varying synchronous error weight coefficients, the two PMSMs are commanded to track an inclined motion trajectory. At 1s, a sudden load is applied to the x-motor, while the y-motor remains unloaded. During the experiment, the synchronous error coefficients of $k_c = 0$, $k_c = 50$, $k_c = 200$, and $k_c = 500$ are employed. The control experiment waveforms during load variation are shown in Fig. 10. The blue solid line and red dashed line represent the response curves of y-motor and x-motor respectively. Fig. 11 shows the comparison of synchronous errors for the different synchronous error coefficients. Table VI summarizes the maximum tracking error on the x-motor ($e_{x\max}$), the maximum tracking error on the y-motor ($e_{y\max}$), the maximum synchronous error ($\epsilon_{\max}$), the average steady-state value of synchronous error ($\epsilon_{\rm rms}$), and the dynamic response time (t_s) under different synchronous error weight coefficients.

The research shows that, when $k_c = 0$, without the inclusion of the synchronous error coefficient, the load on the x-motor did not affect the y-motor, resulting in poor synchronous error performance. As k_c increased from 0 to 50, the y-motor was affected by the load on the x-motor, but the change was relatively small. When the value of k_c further increases from 50 to 500, the influence of the x-motor's load on the y-motor became more pronounced, indicating a stronger coupling effect between the two motors. It can be concluded that as the synchronous error coefficient increases, the synchronous error is significantly reduced from the initial 0.367 rad to 0.058 rad, with a decrease of up to 84.2%; The dynamic response time is remarkably shortened from 0.399 to 0.145 s, with a speed-up effect of 63.7%. However, when $k_c = 500$, the current ripple increases slightly. Therefore, it can be concluded that increasing k_c reduces the synchronous error and accelerates the dynamic response speed, but an excessively large k_c may lead to phenomena such as deteriorated system stability.

F. Robustness Validation Experiments

To validate the control efficacy of the proposed geometric constraint-based predictive position synchronization control strategy for a dual PMSM system under parameter variations, the experiments are conducted where B, J, and ψ_f are each set to 0.5 and 1.5 times their original values. The experimental results showing the tracking of a sinusoidal curve motion trajectory by the dual PMSM system are depicted in Fig. 12.

From Fig. 12, it can be discerned that when B and ψ_f are respectively altered to 0.5 times and 1.5 times of their original magnitudes, the variations in position, velocity, current, and tracking error of the PMSM tracking a sinusoidal curve motion trajectory are negligible. Nevertheless, when J is varied to 0.5 times and 1.5 times of its original value, the tracking error exhibits a certain degree of alteration, indicating that parameter J has a certain influence on the system. Overall, however, the proposed geometric constraint-based predictive position synchronization control strategy for the dual PMSM system demonstrates a certain level of parameter robustness.

G. Verification of Geometric Constraints

In order to validate the efficacy of the constraints within the proposed geometric constraint-based predictive position synchronization control strategy for the dual PMSM system, Fig. 13 illustrates the current limiting effect on the incremental q-axis current during the startup and loading phases of the x-motor. This analysis provides insights into how the control strategy manages current increments, thereby ensuring stable operation and performance under varying conditions.

From Fig. 13, it can be observed that when the x-motor starts, the q-axis current experiences an instantaneous increase. The maximum and minimum current limits act simultaneously on the incremental q-axis current at the moment of motor startup, forming effective constraint boundaries that prevent overcurrent phenomena. Additionally, when a sudden load is applied to the x-motor at 4.78 s, the maximum and minimum current limits also act concurrently on the incremental q-axis current, establishing effective constraint boundaries.

VI. Conclusion

The predictive position synchronization control of dual PMSM system based on geometric constraints proposed in this article has the following advantages.

1) This article adopts the incremental CCS-MPC method to realize multistep prediction. Utilizing its built-in integral action to compensate for the limitation of short control horizons. By calculating the partial derivatives of the established cost function, the unconstrained control increment is obtained, thereby improving the dynamic performance and synchronization control accuracy of the dual-motor system.
2) By solving the geometric constraints, the position of the control increment within the geometric constraint region is first determined. Then, the optimal solution under constrained conditions is obtained through real-time query and calculation of analytical solutions, yielding the control currents for driving the dual PMSMs. This approach effectively reduces the computational load during the solution of quadratic programming algorithms, accelerates the system's convergence speed, and addresses real-time optimization challenges.
3) The control strategy is primarily on providing a lightweight solution method for real-time dual-motor control scenarios. Meanwhile, the experimental verification shows that compared to the traditional QP algorithm, the proposed strategy improves computational efficiency by approximately 47% and dynamic response speed by about 57% while ensuring synchronization control accuracy. It can effectively solve the tradeoff dilemma between accuracy and computational complexity in multimotor synchronization control.

References

[1] C. Gong, Y. R. Li, and N. R. Zargari, "An overview of advancements in multimotor drives: Structural diversity, advanced control, specific technical challenges, and solutions," *Proc. IEEE*, vol. 112, no. 3, pp. 184–209, Mar. 2024.

[2] T. Shi et al., "Review on cooperative control technologies of multi-axis servo systems," in *Proc. Chin. Soc. Elect. Eng.*, Oct. 2024, pp. 1–14.

[3] Z. Liang, S. Hu, Z. Li, and M. Tahir, "Research on master–slave windings motor drive system and control strategy," *IEEE Trans. Ind. Electron.*, vol. 70, no. 1, pp. 88–98, Jan. 2023.

[4] G. Brando, L. Piegari, and I. Spina, "Simplified optimum control method for monoinverter dual parallel PMSM drive," *IEEE Trans. Ind. Electron.*, vol. 65, no. 5, pp. 3763–3771, May 2018.

[5] C. Zhu, Q. Tu, C. Jiang, M. Pan, and H. Huang, "A cross coupling control strategy for dual-motor speed synchronous system based on second order global fast terminal sliding mode control," *IEEE Access*, vol. 8, pp. 217967–217976, Dec. 2020.

[6] S. Wang, J. Su, G. Yang, and G. Sun, "Improved decoupling control with open circuit fault suppression for dual-redundancy permanent magnet synchronous motor," *IEEE J. Emerg. Sel. Topics Power Electron.*, vol. 13, no. 1, pp. 518–530, Feb. 2025.

[7] J. Zhai, W. Wang, X. Wang, and X. Huang, "Multi-motor coordinated propulsion based on improved virtual spindle control," in *Proc. China Automat. Congr.*, Feb. 2024, pp. 1456–1461.

[8] Y. Wu, Y. Cheng, and Y. Wang, "Research on a multi-motor coordinated control strategy based on fuzzy ring network control," *IEEE Access*, vol. 8, pp. 39375–39388, Jan. 2020.

[9] H. Y. Jin and X. M. Zhao, "Dual linear motors servo system synchronization control based on Sugeno type fuzzy neural network and complementary sliding mode controller," *Trans. China Electrotech. Soc.*, vol. 34, no. 13, pp. 2726–2733, 2019.

[10] S. Hu, X. Ren, D. Zheng, and Q. Chen, "Neural network-based robust adaptive synchronization and tracking control for multimotor driving servo systems," *IEEE Trans. Transp. Electrific.*, vol. 10, no. 4, pp. 9618–9630, Dec. 2024.

[11] Z. A. Kuang, H. J. Gao, and M. Tomizuka, "Precise linear-motor synchronization control via cross-coupled second-order discrete-time fractional-order sliding mode," *IEEE/ASME Trans. Mechatron.*, vol. 26, no. 1, pp. 358–368, Feb. 2021.

[12] S. Zou, W. Zhao, C. Wang, W. Liang, and F. Chen, "Tracking and synchronization control strategy of vehicle dual-motor steer-by-wire system via active disturbance rejection control," *IEEE/ASME Trans. Mechatron.*, vol. 28, no. 1, pp. 92–103, Feb. 2023.

[13] W. Shang, F. Xie, B. Zhang, S. Cong, and Z. Li, "Adaptive cross-coupled control of cable-driven parallel robots with model uncertainties," *IEEE Robot. Automat. Lett.*, vol. 5, no. 3, pp. 4110–4117, Jul. 2020.

[14] Z. Y. Jia et al., "A review of contouring-error reduction method in multi-axis CNC machining," *Int. J. Mach. Tools Manuf.*, vol. 125, pp. 34–54, 2018.
[15] Z. Chen, C. Li, B. Yao, M. Yuan, and C. Yang, "Integrated coordinated/synchronized contouring control of a dual-linear-motor-driven gantry," *IEEE Trans. Ind. Electron.*, vol. 67, no. 5, pp. 3944–3954, May 2020.
[16] X. Zhang, T. Shi, Z. Wang, Q. Geng, and C. Xia, "Generalized predictive contour control of the biaxial motion system," *IEEE Trans. Ind. Electron.*, vol. 65, no. 11, pp. 8488–8497, Nov. 2018.
[17] F. Niu et al., "Cooperative predictive position control of dual-motor system," *IEEE J. Emerg. Sel. Topics Power Electron.*, vol. 10, no. 6, pp. 7560–7568, Dec. 2022.
[18] Z. Zhou, S. Zhang, Z. Xu, Y. Peng, and X. Jin, "High-quality positioning strategy for biaxial contour machining system with nonlinear model predictive control," *IEEE J. Emerg. Sel. Topics Power Electron.*, vol. 11, no. 4, pp. 4355–4367, Aug. 2023.
[19] F. Niu, K. Sun, S. Huang, Y. Hu, D. Liang, and Y. Fang, "A review on multi motor synchronous control methods," *IEEE Trans. Transp. Electrific.*, vol. 9, no. 1, pp. 22–33, Mar. 2023.
[20] X. Zhang, Z. Wang, and G. Yang, "Fast position predictive control with current and speed limits for permanent magnet motor systems without weight coefficients," *J. Power Electron.*, vol. 23, no. 4, pp. 625–636, Jan. 2023.
[21] J. Hu, C. He, and Y. Li, "A novel predictive position control with current and speed limits for PMSM drives based on weighting factors elimination," *IEEE Trans. Ind. Electron.*, vol. 69, no. 12, pp. 12458–12468, Dec. 2022.
[22] X. Zhang et al., "Overview of position synchronous control technology for multi-motor system," *Syst. Sci. Control Eng.*, vol. 12, pp. 1–13, Nov. 2024.
[23] L. Sun, X. Li, L. Chen, H. Shi, and Z. Jiang, "Dual-motor coordination for high-quality servo with transmission backlash," *IEEE Trans. Ind. Electron.*, vol. 70, no. 2, pp. 1182–1196, Feb. 2023.
[24] G. Fang, J. Ye, D. Xiao, Z. Xia, and A. Emadi, "Low-ripple continuous control set model predictive torque control for switched reluctance machines based on equivalent linear SRM model," *IEEE Trans. Ind. Electron.*, vol. 69, no. 12, pp. 12480–12495, Dec. 2022.
[25] I. Hammoud et al., "On continuous-set model predictive control of permanent magnet synchronous machines," *IEEE Trans. Power Electron.*, vol. 37, no. 9, pp. 10360–10371, Sep. 2022.
[26] P. Carlet, A. Favato, R. Torchio, F. Toso, S. Bolognani, and F. Dörfler, "Real-time feasibility of data-driven predictive control for synchronous motor drives," *IEEE Trans. Power Electron.*, vol. 38, no. 2, pp. 1672–1682, Feb. 2023.
[27] J. Zhang and Y. G. Xi, "Constraint predictive control direct algorithm based on geometric analysis," *Control Decis.*, no. 2, pp. 184–187, Mar. 1997.
[28] L. Wang *Model Predictive Control System Design and Implementation Using MATLAB*, London, U.K.: Springer, 2009, pp. 43–85.

Xiuyun Zhang was born in Hebei, China, in 1988. She received the B.S. degree in automation from the Hebei University of Technology, City College, Tianjin, China, in 2011, and the M.S. and Ph.D. degrees in control science and engineering from Hebei University of Technology and Tianjin University, Tianjin, China, in 2014 and 2019, respectively.

She is currently a Lecturer with the School of Automation and Electrical Engineering, Tianjin University of Technology and Education, Tianjin, China. Her current research interests include electrical machines, motor drives, and power electronics.

Zhiwei Sun was born in Tianjin, China, in 2000. He received the B.S. degree in automation from Dalian Minzu University, Dalian, China, in 2023. He is currently working toward the M.S. degree in control engineering with the School of Automation and Electrical Engineering, Tianjin University of Technology and Education, Tianjin, China.

His current research interests include motor drives and model predictive control.

Jianyu Chen was born in Guangdong, China, in 2000. He received the B.S. degree in electrical engineering and automation from Guangdong University of Petrochemical Technology, Maoming, China, in 2023. He is currently working toward the M.S. degree in control engineering with the School of Automation and Electrical Engineering, Tianjin University of Technology and Education, Tianjin, China.

His research interests include motor drives and model predictive control.

Zhibiao Zhao was born in Tianjin, China, in 1989. He received the bachelor's degree in measurement, control technology and instruments, and the Ph.D. degree in electronic science and technology from Yanshan University, Hebei, China, in 2012 and 2019, respectively.

He is currently with the School of Automation and Electrical Engineering, Tianjin University of Technology and Education, as a Master's Supervisor. His research interests include modeling and control.

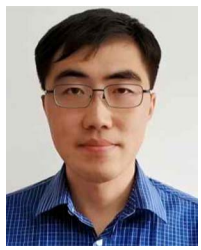

Tao Liu received the B.S., M.S., and Ph.D. degrees in electrical engineering from Tianjin University, Tianjin, China, in 2008, 2010, and 2014, respectively.

He is currently an Associate Professor with the School of Electrical Engineering, Tiangong University, Tianjin, China. His research interests include permanent magnet synchronous motor drive systems, grid-connected converters, and power quality.

Weijie Hou received the B.S. degree in mechatronic engineering from North University of China, Taiyuan, China, in 2010, and the M.S. degree in aeronautical and astronautical science and technology from Beijing Institute of Technology, Beijing, China, in 2015. He is currently working toward the Eng.D. degree in energy and environmental protection with the College of Mechanical and Vehicle Engineering, Hunan University, Changsha, China.

His research interests include microgravity and hypogravity environment simulation technology.